International Journal of Recent Development in Engineering and Technology
Website: www.ijrdet.com (ISSN 2347-6435 (Online) Volume 15, Issue 07, July 2026)

Computational Investigation, ADMET Profiles, Hirshfeld Surface Analysis, And Molecular Dynamics Simulation Of 3a,8a-Dihydroxy-1-Phenyl-2-Thioxo-2,3,3a,8a-Tetrahydro-1H-Indeno[1,2-D]Imidazol-8-One

Tanveer Hasan[1], Sayed Hasan Mehdi[2], Raza Murad Ghalib[3], Pramod Kumar Singh[4], Nazia Kazmi[5], Tazeem[6], Arman Taqvi[7], Syed Asad Ali[8], S. Ali Mehdi Zaidi[9]

[1,8]*Deptt. of Physics, Shia P.G. College, Lucknow-226020, India.*
[2]*Deptt. of Chemistry, Shia P. G. College, Lucknow-226020, India.*
[3,6]*Deptt. of Chemistry, Faculty of Sciences & Arts, Khulais, University of Jeddah, P.O. Box 355, Postal Code 21921 Jeddah, KSA.*
[4]*Deptt. of Applied Physics, SMS Institute, Lucknow, India.*
[5]*Deptt. of Zoology, Shia P.G. College, Lucknow-226020, India.*
[7]*Deptt. of Mathematics, Shia P. G. College, Lucknow-226020, India*
[7,9]*Deptt. of Computer Science, Shia P. G. College, Lucknow-226020, India.*

***Abstract*— We have examined in detail an indeno-imidazole compound entitled with "3a,8a-Dihydroxy-1-phenyl-2-thioxo-2,3,3a,8a-tetrahydro-1H-indeno[1,2-d]imidazol-8-one [(C16H12N2O3S).(H2O)]" [NPTU] bearing anticarcinogenic effect using quantum computational method. The compound's equilibrium geometry has been derived and examined using the DFT-B3LYP/LANL2DZ approach. FT-IR analysis was employed to recognize the different functional groups, and the results are compared with the simulated spectra. Theoretical examination was performed employing the oscillation modes. The electronic characteristics, including HOMO and LUMO energies and the corresponding frontier energy band gap, were determined. Predictions of molecular electrostatic potential surface was carried out to examine the electrophilic and nucleophilic sites. Electrical properties viz. dipole moment, molecular polarizability, and first static hyperpolarizability have been employed to predict the biological characteristics of the molecule. Hirshfeld surface analysis has been done to examine the weak interactions present in the molecules. A molecular dynamics simulation of 100 ns was performed, assessing models through RMSD, RMSF, Rg, PC1-PC2-PLOT metrics, and the MMPBSA/MMGBSA tool was employed for calculating free energy. The drug-likeness and ADMET factors were calculated to examine their medicinal properties.**

***Keywords*—Indeno-imidazole, [(C16H12N2O3S).(H2O)]; Hirshfeld surface; ADMET; DFT; Molecular dynamics simulations.**

I. Introduction

Numerous research advancements have improved cancer prediction. Because it enables experts from many domains to collaborate, the medication development process genuinely represents an interdisciplinary approach.

A novel target for cancer treatment is fusion proteins, which are produced when genes from separate chromosomes unintentionally combine [1]. "3a,8a-Dihydroxy-1-phenyl-2-thioxo-2,3,3a,8a-tetrahydro-1H-indeno[1,2-d]imidazol-8-one [(C16H12N2O3S).(H2O)]" is the compound's title. Our research team produced [NPTU] and detailed both its synthesis and supramolecular chemistry [2]. It comes from indenoimidazole, a bicyclic ring structure consisting of an imidazole ring and an indene ring. These substances are reported to have a variety of biologically significant properties, including anticancer, anticonvulsant, and antiproliferative actions [3-5]. The current work produced various structural and biological properties of the title molecule using Gaussian 09 software and the DFT B3LYP/LANL2DZ technique. To examine the chemical reactivity and reactive sites of the molecule, electronic characteristics such as HOMO, LUMO, frontier orbital energy difference, and molecular electrostatic potential surface (MESP) have been demonstrated. Electrical metrics such as dipole moment, molecular polarizability, and initial static hyperpolarizability have been used to predict the biological properties of the molecule. To assess the pharmacological efficacy, the pharmacokinetic and ADMET properties have also been calculated. Certain weak interactions are revealed by the examination of the Hirshfeld surface and the fingerprint plots that correlate to it. The molecular dynamics simulation analysis have been applied to examine the structural stability of protein-receptor complexes and their binding affinity for the ligand NPTU.

International Journal of Recent Development in Engineering and Technology
Website: www.ijrdet.com (ISSN 2347-6435 (Online) Volume 15, Issue 07, July 2026)

II. Material and Methods

Gaussian 09 software was used to perform quantum chemical calculations for the molecule NPU [6]. In this work, DFT is used in conjunction with the Lee, Yang, and Parr correlation functional and Becke's three-parameter hybrid exchange functional B3LYP [7-9]. In order to calculate vibrational frequencies, electric and electronic parameters, Fukui functions, etc., the optimal geometry has been obtained. The GaussView 6.0 software application was used to create the model molecular structures, HOMO-LUMO, and MESP surfaces for the chemical in question [10]. VEDA 4.0 software was used to calculate the potential energy (PED) distribution for these modes [11]. SWISSADME online program was used to evaluate ADMET and pharmacokinetic properties [12]. The Google Colaboratory platform was used for all of the molecular dynamics simulations [13].

III. Results and Discussion

A. Optimized Molecular Geometry

Molecular geometry usually shows a compound's physical parameters along with its constituent parts, making it possible to investigate these physical parameters. The chemical in question has two benzene rings (R3 and R4), an imidazole ring (R1), and a cyclopentane ring (R2). Energy minimization has been used to optimize the equilibrium geometry for the lowest energy conformer. The optimized geometry of the molecule NPTU is at a minimum on the potential energy surface, as indicated by the computed vibration spectrum's lack of imaginary wave number. Figure 1 shows the compound's optimal configuration, which is comparable to that obtained by X-ray diffraction study.

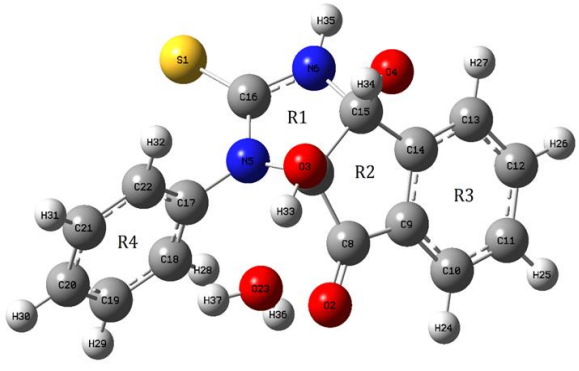

Fig. 1: Optimized geometrical structure of NPTU

The optimized bond lengths of (C-S) are computed at 1.71 Å. The optimized bond lengths of (C-N) are computed within the range of 1.38-1.48 Å.

The bond lengths of (C-H) are determined to be 0.96 to 1.03 Å. The (C-C) stretching is found to be in the range of 1.40-1.58 Å. The (C=O) stretching exhibited a lower value of 1.26 Å in comparison to the (C-O) stretching, which was determined to be in the range of 1.42-1.43 Å. The optimized (O-H) stretching modes were determined at 0.99-1.02 Å. These optimized bond lengths are consistent with the experimental X-ray values presented in supplementary table T1. All the optimized bond angles and dihedral angles aligned well with the experimental data. Consequently, this geometrical data provides a dependable estimate when integrated with experimental crystal data, making the outcomes suitable for calculations of vibrational frequencies.

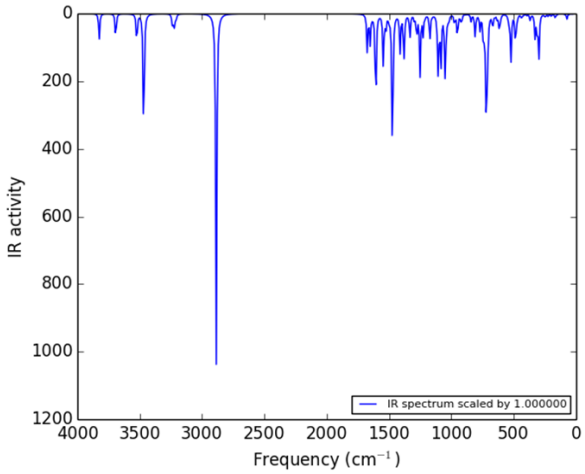

Fig.2: Simulated IR spectrum of NPTU

B. Assignments of Vibrational Modes

The analysed compound, NPTU 37 atoms, thus exhibits 105 vibrational modes. The electron-electron interaction and the an-harmonicity were ignored[14]. The calculated frequencies are at a higher level compared to the experimental values due to these approximations. Consequently, we applied 0.958 to adjust the estimated frequencies to 1700 cm-1 and used 0.9688 for frequencies that are lower [15]. The simulated IR spectra generated using Gaussum 3.0 software are presented in figure 2.

1. stretching

The ν(O-H) vibrations for the title compound are calculated within the frequency range of 3672-3329 cm-1 with 100% to 94% potential energy distribution [PED]. These vibrations manifest as a singular weak absorption peak at 3582 cm-1 in the experimental FTIR spectra.

International Journal of Recent Development in Engineering and Technology
Website: www.ijrdet.com (ISSN 2347-6435 (Online) Volume 15, Issue 07, July 2026)

2. stretching

The sole ν(N-H) stretching vibration of NPTU is computed at a frequency of 3544 cm-1 with a 100% PED.

3. C-H vibrational modes

The ν(C-H) vibrations are predicted to occur within the frequency range of 3110-3067 cm-1. These vibrations manifest as a slight absorption peak seen at 3051 cm-1 in the FTIR spectra, all exhibiting high PED values. The C-H in-plane bending frequencies are extremely useful for characterization and are found in the frequency range of 1500-1000 cm-1 [16]. The calculated frequencies within the range of 1484–1008 cm-1 correspond precisely to the C-H in-plane bending vibrations, appearing as a significant band in the FTIR spectra between 1459 and 1019 cm-1.

4. C=O stretching

The ν (C=O) stretching is estimated at 1608 cm-1, corresponding to a very intense peak at 1600 cm-1 in the FTIR spectrum, with a high PED value.

5. C-C vibrational modes

The ν(C-C) aromatic stretch produces the typical bands in the spectral region of 1600-1000 cm-1 [17]. In the current molecule investigation, ν(C-C) stretching vibrations are detected in FTIR spectra at frequencies 1459 and 1212 cm-1, which are computed by DFT within the frequency range of 1586-1177 cm-1, these modes are combined with the in-plane bending modes.

6. C-N vibrations

The investigation of (C-N) vibrational modes is challenging because they mix with other vibrational modes in the frequency range 1200-1000 cm–1. For NPTU, these are assigned to the experimental frequency peaks in the spectrum at 1212 cm–1 and are estimated within the frequency range of 1245-1040 cm-1.

7. (S-C) vibrational modes

The out-of-plane bending modes of (C–S) are computed in the range 642 -592 cm^{-1}, whereas the (C–S) stretching modes are computed at 405 and 403 cm^{-1}. The experimental value for this vibrational mode is assigned at 658 cm^{-1}. These vibrational modes are usually found in the range of 600- 750 cm^{-1} in the literature [16].

8. Modes in the lower spectral region

Investigation of low-frequency vibrational modes is crucial because it sheds light on the weak intermolecular interactions that occur during enzyme activities [17].

The interpretation of the impact of electromagnetic radiation on biological systems can also benefit from the knowledge of low-frequency modes [18]. Several torsional modes are obtained in the lower-middle region of the experimental FTIR spectrum and are well matched with the computed values. The table includes the list of each of these modes comprising several peaks in the experimental spectra at frequencies 749, 729, 711 and 697 cm–1 and are optimized in the range 765 and 755 cm–1 respectively. These seem to be the characteristic modes for the title compound NPTU.

C. Frontier molecular orbital analysis and electronic parameters

HOMO and LUMO have been extensively employed to understand the reactivity and area selectivity of various chemical compounds. A narrower HOMO and LUMO gap suggest a more unstable and softer molecular structure, whereas a wider energy gap signifies a more stable and harder molecular structure. The soft molecules are typically unstable and relatively prone to chemical reactions [19, 20].

Figure 3 illustrates the 2D representations of the HOMO and LUMO for the title compound NPTU. It shows that the major part of the HOMO is concentrated on the Sulphur atom S1 and at some portion of the imidazole ring R1, while the LUMO is distributed across the cyclopentene ring R2 and the benzene ring R3. Consequently, charge transfer takes place from the Sulphur atom S1 and ring R1 to the rings R2 and R3. The calculated HOMO-LUMO energy gap of 2.805 eV indicates that the title compound NPU has a high degree of polarizability and chemical reactivity, thus categorizing it as a soft molecule [21, 22].The molecular electrostatic plot (MESP) for the title compound NPTU is shown in figure 4. It is evident from the figure 4, that the least reactive portion is of the Sulphur atom S1 as it is the most covered area with the MESP. The benzene ring R4 is possibly the most reactive portion, as it possesses the smallest covered area with MESP. Additionally, the area surrounding the ring R4 is deficient in electrons (represented by the minimum electrostatic potential in blue), providing binding sites for nucleophilic attack. The region with high electron density (maximum electrostatic potential represented in red) is primarily located over the imidazole ring R1 and the cyclopentene rings R2, making them a very active site for electrophilic attack.

International Journal of Recent Development in Engineering and Technology
Website: www.ijrdet.com (ISSN 2347-6435 (Online) Volume 15, Issue 07, July 2026)

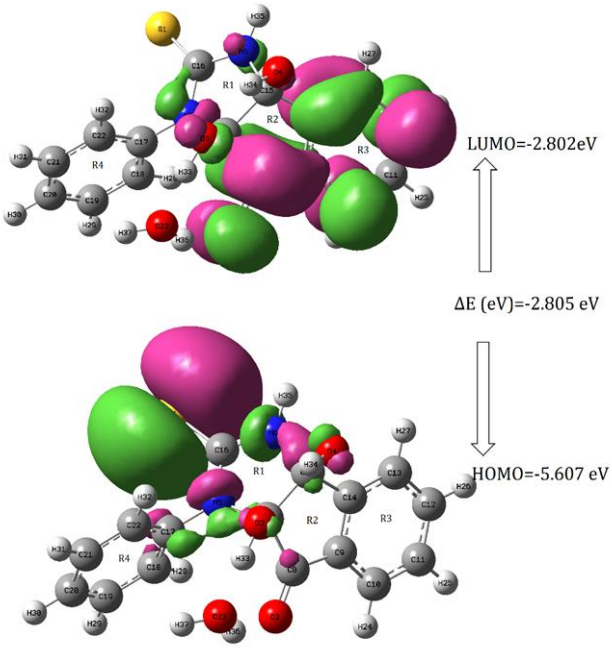

Fig.3: 2D-HOMO-LUMO plot of NPTU

Table I : Electronic parameters of NPTU

Parameters	DFT-Values(eV)
E_{HOMO} (eV)	-5.61
E_{LUMO} (eV)	-2.801
ΔE (eV)	2.805
Ionization potential (I)	5.61
Electron affinity(A)	2.801
Electronegativity(χ)	4.2055
Chemical potential(μ)	-4.2055
Chemical hardness(η)	1.4045
Global softness(S)	0.356
Electrophilicity index (ω)	6.29

A number of calculated electronic characteristics that characterize the overall reactivity of the molecule are shown in Table I. The results showed that the ionization potential was estimated as 5.61 eV, the electron affinity as 2.801 eV, the electronegativity as 4.2055 eV, and the chemical hardness as 1.4045 eV. Therefore, the title molecule should have sufficient biological activity, according to these criteria and the electrophilicity levels (6.29 eV).

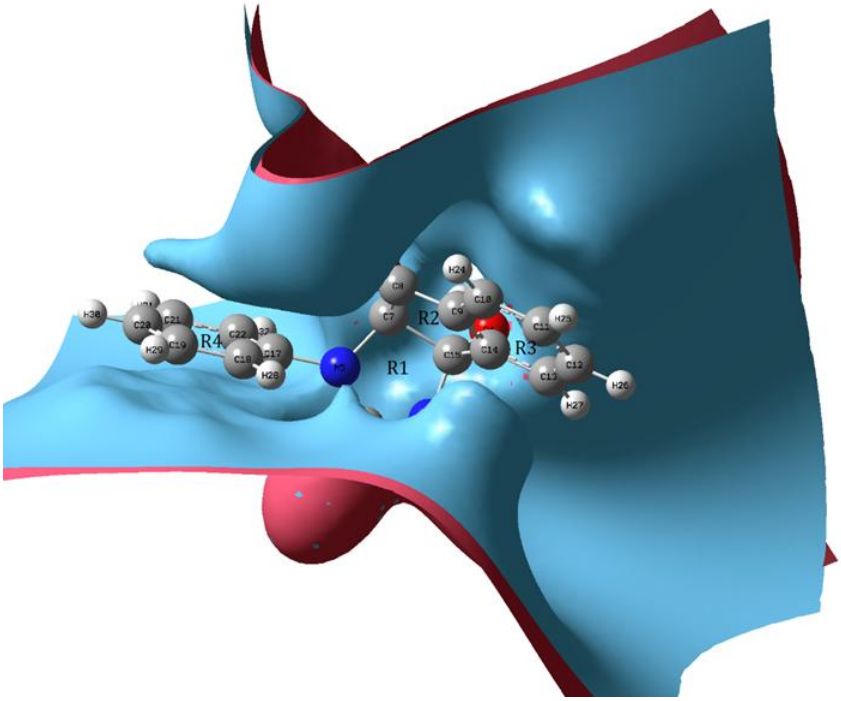

Fig. 4 2D MESP plot of NPTU

International Journal of Recent Development in Engineering and Technology
Website: www.ijrdet.com (ISSN 2347-6435 (Online) Volume 15, Issue 07, July 2026)

Additionally, the area surrounding the ring R4 is deficient in electrons (represented by the minimum electrostatic potential in blue), providing binding sites for nucleophilic attack. The region with high electron density (maximum electrostatic potential represented in red) is primarily located over the imidazole ring R1 and the cyclopentene rings R2, making them a very active site for electrophilic attack.

A number of calculated electronic characteristics that characterize the overall reactivity of the molecule are shown in Table I. The results showed that the ionization potential was estimated as 5.61 eV, the electron affinity as 2.801 eV, the electronegativity as 4.2055 eV, and the chemical hardness as 1.4045 eV. Therefore, the title molecule should have sufficient biological activity, according to these criteria and the electrophilicity levels (6.29 eV).

D. Electrical parameters

The dipole moment of the NPTU molecule is aligned in the Y-Z plane, with calculated values of 4.47 D.

The α_{YY} and α_{ZZ} components has a greater contribution to the mean polarizability $<\alpha>$ than the α_{XX} component, which accounts for their greater elongation along the Y-Z-axes. The average polarizability $<\alpha>$ was recorded at -133.61 a.u., suggesting that it is likely to show adequate biological activity.

Table II outlines various relevant electric parameters, such as dipole moment, polarizability, and first-order hyperpolarizability for the molecule. Organic compounds with an (N-H) group exhibit increased molecular hyperpolarizability and mechanical stability because of the presence of hydrogen bond interactions. Furthermore, the first-order hyperpolarizability correlates with the energy band gap that exists between the HOMO and LUMO. Consequently, a wider band gap is associated with a reduced first hyperpolarizability. The calculated first-order hyperpolarizability βtotal is 0.107 x 10-30 e.s.u., which is less than the benchmark compound Urea (βtotal = 0.3728 x 10-30 e.s.u.), suggesting that it is not appropriate for nonlinear optical (NLO) purposes [23, 24].

Table II: Electric parameters for NPTU by DFT

Components	NPTU	Components	Hyperpolarizability (e.s.u. *10-33)
αxx	-107.36	βXXX	12.36
αxy	14.37	βXXY	-44.74
αyy	-152.46	βXYY	29.48
αxz	-11.93	βYYY	-42.86
αyz	9.92	βxxz	-25.37
αzz	-141.00	βXYZ	0.88
<α>	**-133.61**	βYYZ	12.00
		βXZZ	-20.37
Electric Dipole moment (μ) (D)	**4.47**	βYZZ	-17.75
		βZZZ	7.22
		β1	460.53
		β2	11098.71
		β3	37.85
		βtotal	**107.69**

E. Characteristics of Drug Likeness and ADME Profiles

ADME profiles and drug likeness metrics were assessed utilizing PreADME and SWISSADME online tools for the compound under investigation and are shown in Table III. The Lipinski rule of 5 (LiR of 5) helps to distinguish between drug-like and non-drug-like molecules.

The calculated values for drug likeness parameters of the title compound are: (i) HBD is 4 (≤5), (ii) HBA is 4 (≤10), (iii) MW is 330.36 g/mol (≤500 g/mol), (iv) MR is 93.84 (40-130 cm^3 mol^{-1}) and (v) log P is 1.3 (0-5), suggesting excellent permeability through biological membranes and advantageous binding to plasma proteins [25-27].

International Journal of Recent Development in Engineering and Technology
Website: www.ijrdet.com (ISSN 2347-6435 (Online) Volume 15, Issue 07, July 2026)

The van der Waals topological polar surface area (TPSA) of the compound is 114.12 Å², which is less than 120 Å².The partition coefficient (Milog P) is 0.75, which is within the range of ≤5.Based on these values, it is evident that the compound NPTU surpasses the LiR of 5 and is therefore considered suitable for in vivo testing. In terms of ADME parameters, the human intestinal absorption (HIA) value represents the combined absorption and bioavailability derived from the excretion through urine, bile, and feces, with a calculated value of 90.0245% [28, 29]. CaCo-2 is a cell line derived from human colon epithelial tissue and is frequently used as a model to evaluate drug absorption in the human digestive system. The calculated value of 20.97 falls within the acceptable range of [13.0–76.7 nm/s], indicating improved intestinal absorption. Madin Darby Canine Kidney (MDCK) cells are commonly used in vitro to determine the permeability of drug candidates, offering insights into their potential absorption in the gastrointestinal tract and across the blood-brain barrier. Drug permeability through MDCK cell monolayers is typically measured in nm/s and is used to classify the drug's absorption capacity, as MDCK cells grow faster than CaCo-2 cells [30].

Table III: Drug Likeness, ADME parameters of NPTU

S.No.	Drug Likeness parameters		S.No.	ADME parameters	
	Parameters	NPU		Parameters	NPU
1	Formula	$C_{16}H_{14}N_2O_4S$	16	GI absorption	High
2	MW	330.36	17	BBB permeant penetration (c.brain/ c.blood)	1.084(no)
3	Bioavailability Score	0.55	18	Lipinski Violations(LiR5)	0
4	Rotatable bonds(RBs)	1	19	Caco-2 cell permeability (nm/s)	20.9732
5	Heavy atoms	23	20	CYP_2C9_inhibition	Non
6	Aromatic heavy atoms	12	21	CYP_2D6_inhibition	Non
7	Fraction Csp3	0.12	22	CYP_2D6_substrate	Non
8	H-bond acceptors(HBA)	4	23	CYP_3A4_inhibition	Non
9	H-bond donors(HBD)	4	24	CYP_3A4_substrate	Weakly
10	MR	93.84	25	HIA (%)	90.0245
11	TPSA	114.12	26	MDCK cell permeability (nm/s)	174.46
12	iLOGP	1.92	27	Pgp_inhibition	Inhibitor
13	MLOGP	0.75	28	Plasma_Protein_Binding	91.504
14	ESOL Log S	-2.6	29	Pure_water_solubility_mg/L	10.724
15	Ali Log S	-2.59	30	Skin_Permeability (log Kp)	-3.414

International Journal of Recent Development in Engineering and Technology
Website: www.ijrdet.com (ISSN 2347-6435 (Online) Volume 15, Issue 07, July 2026)

The permeability measurement for MDCK cells was found to be 174.46 nm/s [25–500 nm/s], which is suitable for elimination by renal cells. The computed skin permeability value for NPTU is -3.414 (log Kp < -4), indicating that the compound does not penetrate the skin.</mark> The plasma protein binding value is 91.50, which is within the range of <80% PPB <99, suggesting strong binding with blood plasma.</mark> The inability of NPTU to inhibit CYP3A4, CYP2D6, CYP2C9, and CYP2C19 indicates that the molecule requires xenobiotic metabolism in the body. Typically, a molecule with 10 or fewer rotatable bonds (RBs) is considered to have favorable drug-like properties. NPTU has only 1 rotatable bond. In both in vitro and in silico evaluations of drug-like properties, the expected pharmacokinetic parameters and physicochemical characteristics known as Lipinski's rules are important [31, 32].

F. Toxicity predictions

Assessing toxicity is crucial in drug development and aids in recognizing harmful effects of new medications on the body.

The toxicity of the compound NPTU was assessed using the ProTox-II online software [33]. The findings of organ toxicity indicated that NPTU was forecasted to be hepatotoxic, respiratory, and clinical toxic.

The results for toxicity endpoints indicated that NPTU shows activity regarding the blood-brain barrier and clinical toxicity. The CNS-active compounds consistently cross the Blood–Brain Barrier (BBB) and produce secondary effects in the CNS [34, 35]. The title compound demonstrated inactivity for molecular initiation events across all parameters, including the GABA receptor. All the toxicity parameters are provided in the table IV.

Table IV: Prediction of Toxicity of NPTU using ProTox-3.0 software

Classification	Target	Shorthand	Prediction	Probability
Organ toxicity	Hepatotoxicity	dili	Active	0.61
Organ toxicity	Neurotoxicity	neuro	Inactive	0.51
Organ toxicity	Nephrotoxicity	nephro	Inactive	0.50
Organ toxicity	Respiratory toxicity	respi	Active	0.78
Organ toxicity	Cardiotoxicity	cardio	Inactive	0.87
Toxicity end points	Carcinogenicity	carcino	Inactive	0.66
Toxicity end points	Immunotoxicity	immuno	Inactive	0.99
Toxicity end points	Mutagenicity	mutagen	Inactive	0.65
Toxicity end points	Cytotoxicity	cyto	Inactive	0.64
Toxicity end points	BBB-barrier	bbb	Inactive	0.52
Toxicity end points	Ecotoxicity	eco	Inactive	0.55
Toxicity end points	Clinical toxicity	clinical	Active	0.59
Toxicity end points	Nutritional toxicity	nutri	Inactive	0.56
Tox21-Nuclear receptor signalling pathways	Aryl hydrocarbon Receptor (AhR)	nr_ahr	Inactive	0.66
Tox21-Nuclear receptor signalling pathways	Androgen Receptor (AR)	nr_ar	Inactive	0.96
Tox21-Nuclear receptor signalling pathways	Androgen Receptor Ligand Binding Domain (AR-LBD)	nr_ar_lbd	Inactive	0.96
Tox21-Nuclear receptor signalling pathways	Aromatase	nr_aromatase	Inactive	0.80
Tox21-Nuclear receptor signalling pathways	Estrogen Receptor Alpha (ER)	nr_er	Inactive	0.82
Tox21-Nuclear receptor signalling pathways	Estrogen Receptor Ligand Binding Domain (ER-LBD)	nr_er_lbd	Inactive	0.96

International Journal of Recent Development in Engineering and Technology
Website: www.ijrdet.com (ISSN 2347-6435 (Online) Volume 15, Issue 07, July 2026)

Tox21-Nuclear receptor signalling pathways	Peroxisome Proliferator Activated Receptor Gamma (PPAR-Gamma)	nr_ppar_gamma	Inactive	0.87
Tox21-Stress response pathways	Nuclear factor (erythroid-derived 2)-like 2/antioxidant responsive element (nrf2/ARE)	sr_are	Inactive	0.88
Tox21-Stress response pathways	Heat shock factor response element (HSE)	sr_hse	Inactive	0.88
Tox21-Stress response pathways	Mitochondrial Membrane Potential (MMP)	sr_mmp	Inactive	0.60
Tox21-Stress response pathways	Phosphoprotein (Tumor Suppressor) p53	sr_p53	Inactive	0.71
Tox21-Stress response pathways	ATPase family AAA domain-containing protein 5 (ATAD5)	sr_atad5	Inactive	0.84
Molecular Initiating Events	Thyroid hormone receptor alpha (THRα)	mie_thr_alpha	Inactive	0.83
Molecular Initiating Events	Thyroid hormone receptor beta (THRβ)	mie_thr_beta	Inactive	0.79
Molecular Initiating Events	Transtyretrin (TTR)	mie_ttr	Inactive	0.59
Molecular Initiating Events	Ryanodine receptor (RYR)	mie_ryr	Inactive	0.89
Molecular Initiating Events	GABA receptor (GABAR)	mie_gabar	Inactive	0.91
Molecular Initiating Events	Glutamate N-methyl-D-aspartate receptor (NMDAR)	mie_nmdar	Inactive	0.93
Molecular Initiating Events	alpha-amino-3-hydroxy-5-methyl-4-isoxazolepropionate receptor (AMPAR)	mie_ampar	Inactive	0.93
Molecular Initiating Events	Kainate receptor (KAR)	mie_kar	Inactive	0.95
Molecular Initiating Events	Achetylcholinesterase (AChE)	mie_ache	Inactive	0.94
Molecular Initiating Events	Constitutive androstane receptor (CAR)	mie_car	Inactive	1
Molecular Initiating Events	Pregnane X receptor (PXR)	mie_pxr	Inactive	0.64
Molecular Initiating Events	NADH-quinone oxidoreductase (NADHOX)	mie_nadhox	Inactive	0.99
Molecular Initiating Events	Voltage gated sodium channel (VGSC)	mie_vgsc	Inactive	0.65
Molecular Initiating Events	Na+/I- symporter (NIS)	mie_nis	Inactive	0.91
Metabolism	Cytochrome CYP1A2	CYP1A2	Inactive	0.86
Metabolism	Cytochrome CYP2C19	CYP2C19	Inactive	0.88

International Journal of Recent Development in Engineering and Technology
Website: www.ijrdet.com (ISSN 2347-6435 (Online) Volume 15, Issue 07, July 2026)

Metabolism	Cytochrome CYP2C9	CYP2C9	Inactive	0.60
Metabolism	Cytochrome CYP2D6	CYP2D6	Inactive	0.88
Metabolism	Cytochrome CYP3A4	CYP3A4	Inactive	0.86
Metabolism	Cytochrome CYP2E1	CYP2E1	Inactive	1

G. Hirshfeld surface analysis

Hirshfeld surface illustrating weak intermolecular interactions in the crystal structure is represented over dnorm for NPTU using the crystal structure file (cif) as input, shown in fig. 5. The Crystal Explorer 21 software is utilized to generate Hirshfeld surfaces and 2D fingerprint diagrams [37]. Fig 5(a) clearly shows that the title compound has three robust hydrogen bonds. H1N2 (2.636 Å), H1O3 (2.449 Å) and H2W1 (1.099 Å) with adjacent molecules marked by red dots on the dnorm surface.

The weak interactions are represented in blue, while the absence of interactions is depicted in grey on the 2D crystal surface in figure 5. To enhance the comprehension of weak interactions, 2D fingerprint representations of the compound have been created and are displayed in fig. 5 (b to g). They illustrate the roles of individual All-interactions, All-H, H--C, S--C, H--O and All--O interactions in the total interactions respectively.

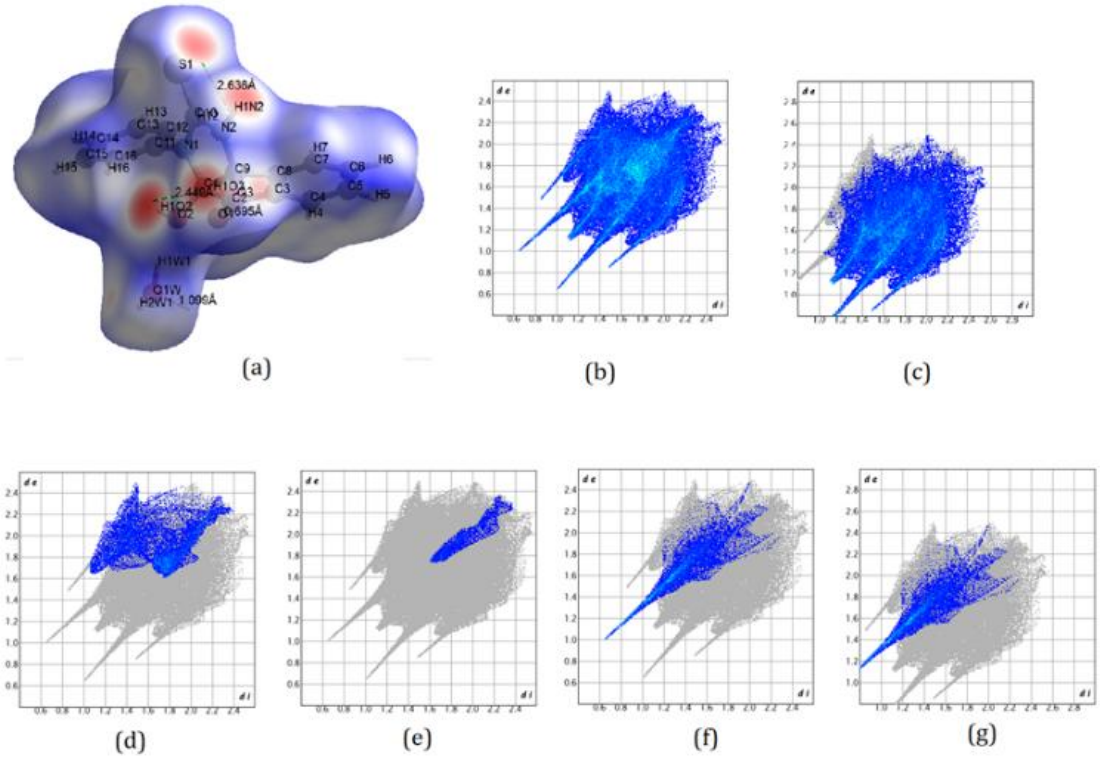

Fig. 5. (a) 2D crystal surface of NPTU (b) All interactions (c) H-H (d) H–C (e) S--C (f) H—O (g) All-O

International Journal of Recent Development in Engineering and Technology
Website: www.ijrdet.com (ISSN 2347-6435 (Online) Volume 15, Issue 07, July 2026)

H. Molecular Dynamics Simulations

1. RMSD Analysis

The root mean square deviation (RMSD) technique was employed to examine the structural behavior of ligands in the active region of proteins. Figure 6(a) and (b) display the RMSD plots for the examined ligand, NPTU, in relation to the two protein receptors, 4WNT and 4XRZ, respectively.

For NPTU-4WNT ligand-protein receptor combination RMSD value initially rises from 0.7 Å to 2.2 Å then fluctuates between 1.25 to 2.7 Å and it finally stabilized at 2.0 Å. For the NPTU-4XRZ, combination, the value of RMSD consistently rises over time, reaching a peak of σ = 3.9 Å at 68 ns and then fluctuating between 3.5 and 2.5 Å before finally settling at 2.0 Å at 100 ns.

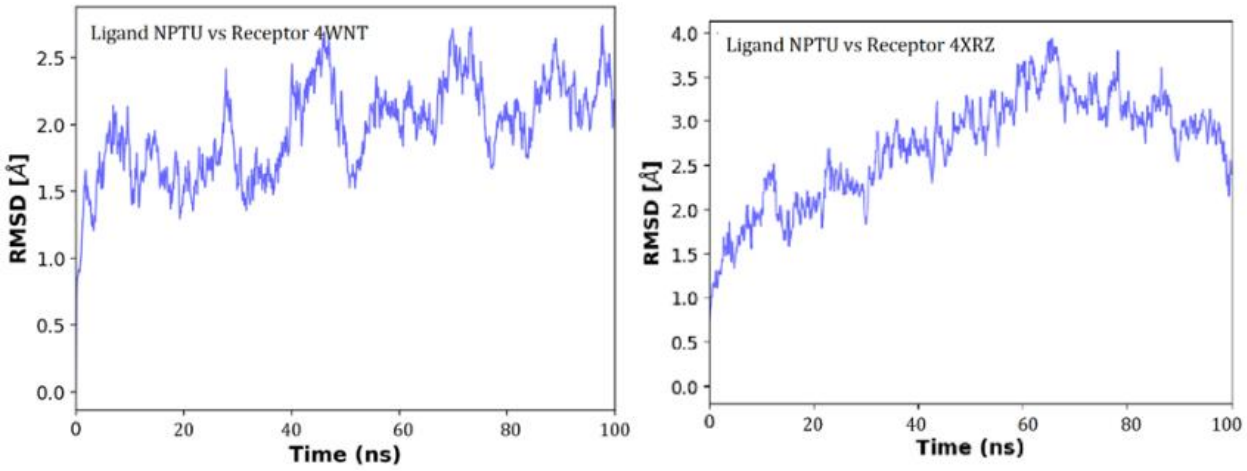

Fig. 6: RMSD fluctuations of NPTU with the protein receptors (a) 4WNT and (b) 4XRZ

2. Root Mean Square Fluctuations

Figures 7(a) and 7(b) display the root mean square (RMS) fluctuations of the title molecule interacting with the two receptor proteins, 4XRZ and 4WNT, respectively.

The comparative data indicates that the RMS fluctuations are highest between the residues with 200-700 atoms, presenting values ranging from 0.50 to 3.25, respectively.

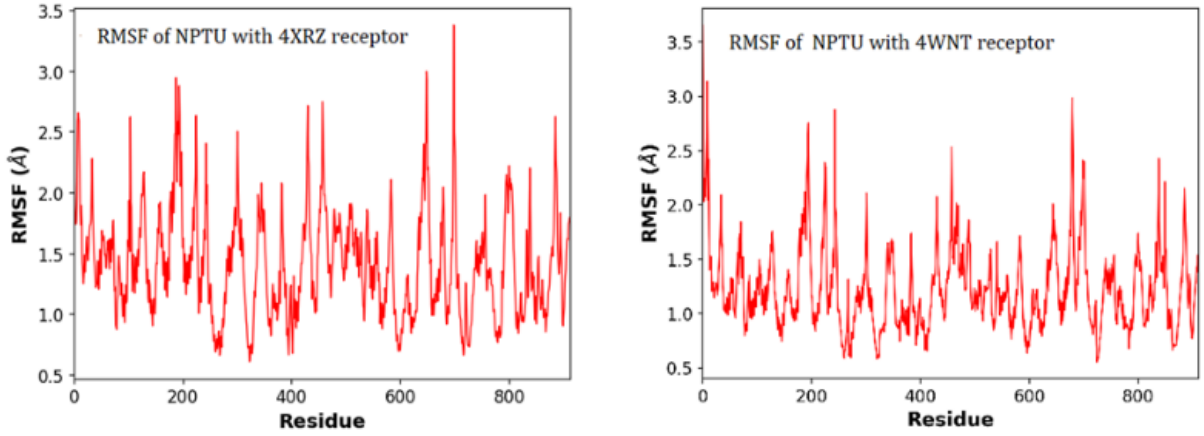

Fig. 7: RMS fluctuations of NPU with the proteins (a) 4XRZ and (b) 4WNT

International Journal of Recent Development in Engineering and Technology
Website: www.ijrdet.com (ISSN 2347-6435 (Online) Volume 15, Issue 07, July 2026)

For the NPTU-4XRZ combination, the RMS starts fluctuation from 1.75 Å reaching maximum at 700 residue number and finally stabilizing at 1.75 Å for residue 1000. For the NPTU-4WNT ligand-protein combination, the RMS starts fluctuation from 2.0 Å reaching maximum within no time and finally stabilizing at 1.50 Å for residue 1000.

3.Radius of Gyration (R_g)

The radius of gyration (Rg) can be used to calculate the structural compactness of a protein structure.

The graphical representations of Rg can help assess the rigidity level of a protein structure. Throughout the 100 ns simulation duration, well-folded proteins show relatively stable values, while misfolded or unstable proteins display variations. The 2D plot in figure 8(a) for NPTU-4WNT indicates that, Rg fluctuates 33.1 to 33.9 Å before stabilizing at 33.5 Å after 90 ns. For the NPTU-4XRZ combination Rg start fluctuating from 33.7 Å, reaches to maximum value 34.1 Å and minimum value 33.1 Å before finally stabilizing at 33.9 Å.

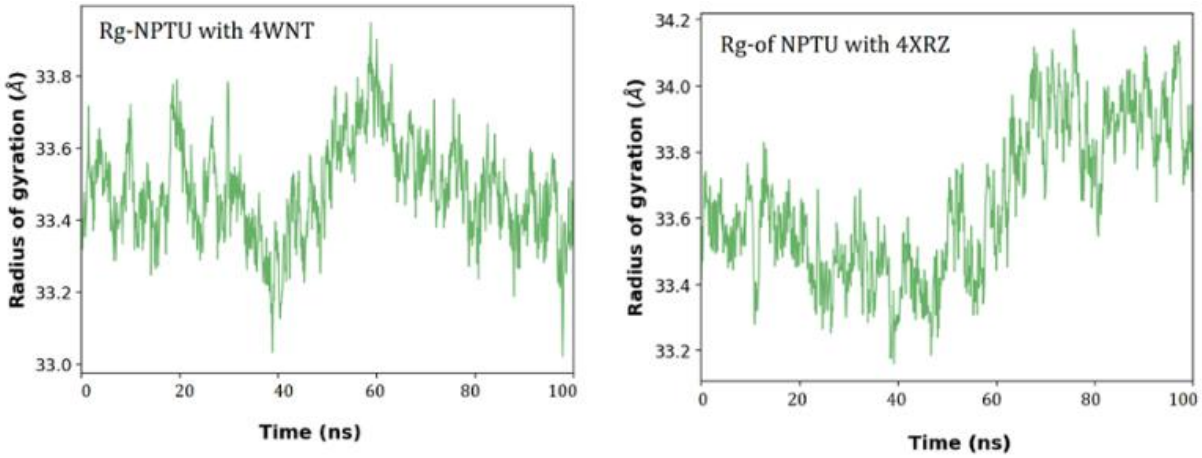

Fig. 8: Radius of gyration (Rg) of the ligand NPU with the proteins (a) 4WNT and (b) 4XRZ

4. PC1 and PC2 projections

Principal component analysis is commonly utilized as a method in exploratory data analysis to uncover the underlying data structure in a manner that most effectively elucidates its variance. When applied to a collection of snapshots from an MD trajectory, the PCs illustrate collective atomic movements and can emphasize significant conformational alterations between the structures [37,38]. Figures 9(a) and (b) show two-dimensional projections of PC1 and PC2 for the ligand NPTU with the proteins 4WNT and 4XRZ over the duration of 100 ns MD simulations.

The green hue signifies anti-correlated movement, whereas the pastel shade indicates correlated movement. In the graph-1(fig 9a), in the early-stage trajectory (0 to ~40 ns), the data points occupy the right hemisphere, clustered tightly between PC1 values of +20 and +60, and PC2 values of 0 to +40. In mid-stage transition (~40 to ~70 ns), the trajectory shifts downward and leftward into the bottom-center region, centering around PC1 ≈ 0 and PC2 ≈ -30. Then in the late-stage trajectory (~70 to 100 ns), the structure settles into a stable, highly populated cluster on the far left, spanning PC1 values of -20 to -60 and PC2 values of -20 to +40. The protein follows a linear or sweeping continuous path from right to bottom-center, then up to the left.

International Journal of Recent Development in Engineering and Technology
Website: www.ijrdet.com (ISSN 2347-6435 (Online) Volume 15, Issue 07, July 2026)

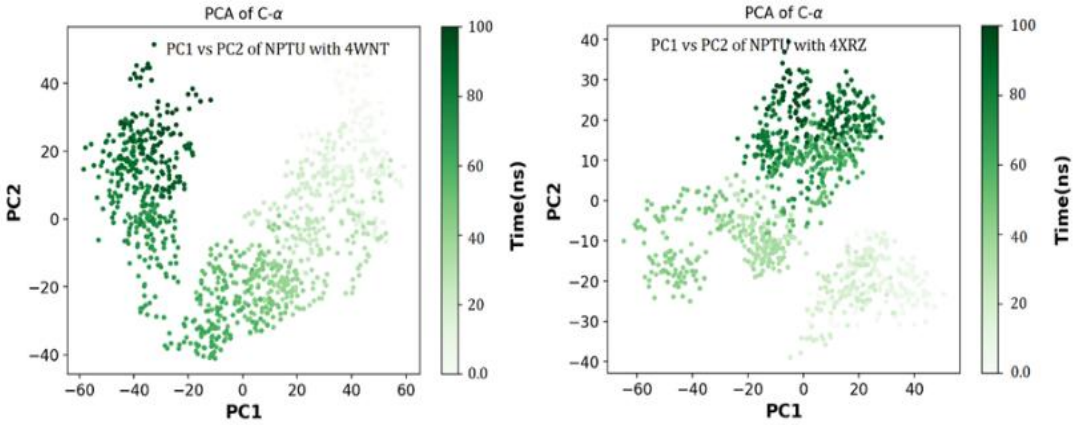

Fig. 9. 2D-Projection's trajectories PC1 & PC2 of the ligand NPU with the protein receptors (a) 4WNT and (b) 4XRZ

In the graph 2 (fig 9b), in the early-stage trajectory (0 to ~30 ns), the conformations begin in the bottom-right quadrant, centered around PC1 values of 0 to +40 and PC2 values of -35 to -10. In mid-stage transition (~30 to ~60 ns), the system travels over to the left hemisphere, populating a loose cluster spanning PC1 values of -20 to -60 and PC2 values of -25 to 0. In the late-stage trajectory (~60 to 100 ns); the structure migrates upward into the top-center/top-right region, forming a dense cluster between PC1 values of -20 to +30 and PC2 values of +10 to +35. The protein follows a distinct triangular or clockwise-like loop through the conformational phase space.

5. Interaction Energy

The interaction energies throughout the simulation process are illustrated in figures 10(a) and 10(b) for the ligand and the two protein receptors, 4WNT and 4XRZ, respectively. The graphical depiction distinctly shows that Van der Waal energy is crucial in comparison to the electrostatic energy regarding the total interaction energy of the system. For both proteins, the total interaction energies remain negative for the majority of the simulation duration, ultimately stabilizing at a negative value, indicating that both ligand-protein complexes were stabilized.

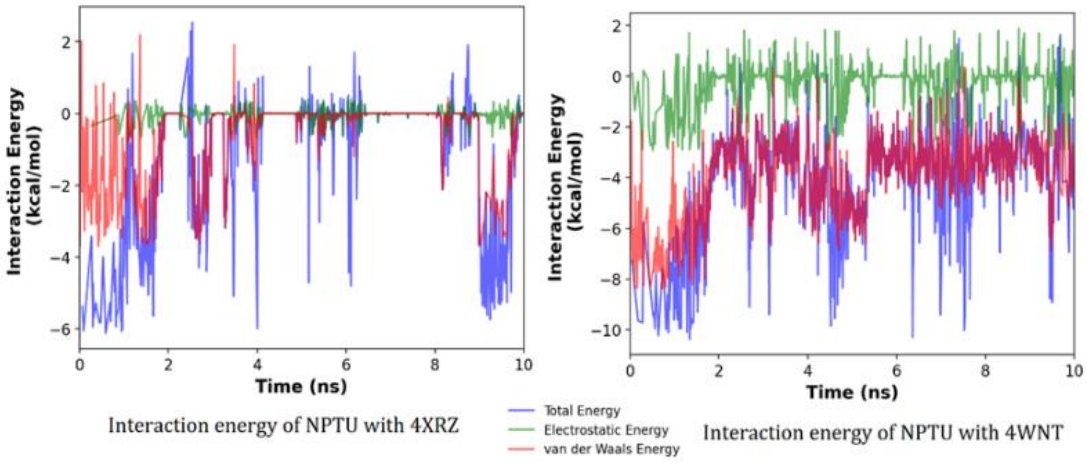

Fig. 10. Interaction energies for NPTU with the receptors (a) 4XRZ (b) 4WNT

International Journal of Recent Development in Engineering and Technology
Website: www.ijrdet.com (ISSN 2347-6435 (Online) Volume 15, Issue 07, July 2026)

6. MMPBSA/MMGBSA analysis

Molecular Mechanics/Poisson-Boltzmann Surface Area (MMPBSA) and Molecular Mechanics/Generalized Born Surface Area were used to calculate the binding free energy for the protein-ligand couples by examining 1000 end-frames. When compared to MMGBSA, reports show that the MMPBSA approach balances computational efficiency and accuracy, particularly when used on bigger systems [39]. Using Gromacs trajectory and topology files, the MMPBSA and MMGBSA programs were utilized to calculate free energy.

DAT (.dat) and CSV (.csv) formats were used to hold the results, and an index file was first produced. Figures 11(a) and (b) for each of the two proteins-ligand complexes illustrate how the MMPBSA and MMGBSA modules were used to record all energetic contributions and the total variance in binding energy throughout 100 ns simulations.

It is evident from these graphs that total energy difference as computed by MMPBSA module is larger than MMGBSA for both the protein-ligand complexes.

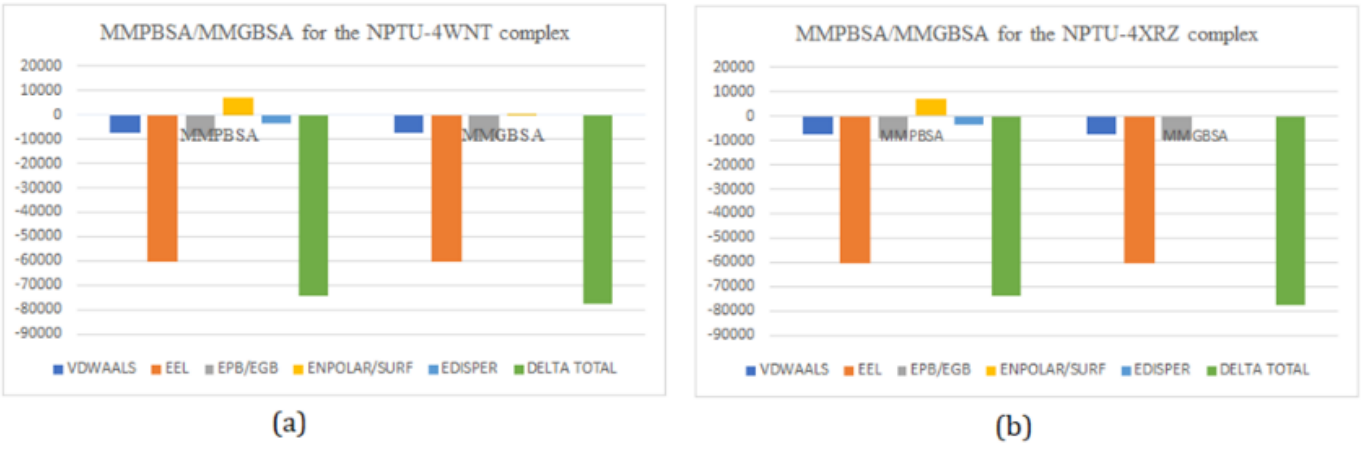

Fig. 11: Free energy values employing the MMPBSA/MMGBSA modules for NPTU with 4WNT and 4XRZ

IV. Conclusions

Using the DFT-B3LYP/LANL2DZ method, a theoretical quantum chemical study of 3a,8a-Dihydroxy-1-phenyl-2-thioxo-2,3,3a,8a-tetrahydro-1H-indeno[1,2-d]imidazol-8-one [(C16H12N2O3S).(H2O)] was carried out. The computed and observed normal modes of vibrations showed a strong correlation. The molecule's biological characteristics were made clear by the electric descriptions. The title compound's remarkable polarizability and chemical reactivity are demonstrated by the HOMO LUMO plot and its tiny frontier energy gap (2.805 eV). The molecule in issue is predicted to have sufficient biological activity based on the computed electronic characteristics, especially the electrophilicity levels (6.29 eV). The presence of hydrogen bonding contacts was indicated by unique peaks in the fingerprint plots, which were also seen in the molecular dynamics, according to Hirshfeld surface analysis.

Several factors have been computed employing molecular dynamics analysis.

The stability of the ligand-protein complexes is indicated by the RMSD values of 2Å and 2.2 Å, which are between 2 and 3 Å; the RMSF values of 1.5 and 1.75 Å, which are both between 1.5 and 3 Å; the Rg values are calculated as 33.5 and 33.9 Å, which are also close to the stability range (between 15 and 30 Å); PC1 & PC2 used in Principal Component Analysis (PCA) are calculated to capture essential protein motions, map free energy landscapes, and compare drug-binding stability, along with interaction energies.

The title molecule satisfied Lipinski's drug similarity criteria and showed encouraging ADMET properties. These discoveries could result in the creation of more novel physiologically active substances with imidazole rings.

Supporting Information.

The table for the optimized parameters [T1], table for the vibrational assignments [T2] and for the table for the toxicity of the title compound NPTU have been provided in the "supplementary information file".

Acknowledgments.

The help received from Prof. Neeraj Misra; Department of Physics University of Lucknow is highly acknowledged.

Conflict of Interest.

Authors declare that there is no conflict of interest for this manuscript.

REFERENCES

[1] Mertens, F.; Johansson, B.; Fioretos, T.; Mitelman, F.Nat. Rev. Cancer 2015, 15, 371.

[2] Ghalib, R. M, Mehdi, S. H, Hashim, R, Alshahateet S. F, Sulaiman, O, *J. Chem. Sci.* Vol. 128, No. 12, December 2016, pp. 1841–1847.

[3] Sarkarzadeh H, Miri R, Firuzi O, Amini M, Razzaghi Asl N, Edraki N and Shafiee, A 2013 *Arch. Pharm. Res*. 36, 436.

[4] Chatterjie N, Sinha B and Alexander G J, 1983, *Res. Commun. Chem. Pathol. Pharmacol*. 39 333.

[5] Roberts L R, Bryans J, Conlon K, McMurray G, Stobie A, Whitlock G A, 2008, *Bioorg. Med. Chem. Lett.* 18, 6437.

[6] Frisch, M. J.; Trucks, G. W.; Schlegel, H. B.; Scuseria, G.E.; Robb, M. A.; Cheeseman, J. R.; Montgomery, Jr., J.A.; Vreven, T.; Kudin, K. N.; Burant, J. C.; Millam, J. M.; Iyengar, S. S.; Tomasi, J.; Barone, V.; Mennucci, B.; Cossi, M.; Scalmani, G.; Rega, N.; Petersson, G. A.; Nakatsuji, H.; Hada, M.; Ehara, M.; Toyota, K.; Fukuda, R.; Hasegawa, J.; Ishida, M.; Nakajima, T.; Honda, Y.;Kitao, O.; Nakai, H.; Klene, M.; Li, X.; Knox, J. E.; P. Hratchian, H.; Cross, J. B.; Adamo, C.; Jaramillo, J.; Gomperts, R.; Stratmann, R. E.; Yazyev, O.; Austin, A. J.; Cammi, R.; Pomelli, C.; Ochterski, J. W.; Ayala, P. Y.; Morokuma, K.; Voth, G. A.; Salvador, P.; Dannenberg, J. J.; Zakrzewski, V. G.; Dapprich, S.; Daniels, A. D.; Strain, M. C.; Farkas, O.; Malick, D. K.; Rabuck, A. D.; Raghavachari, K.; Foresman, J. B.; Ortiz, J. V.; Cui, Q.; Baboul, A. G.; Clifford, S.; Cioslowski, J.; Stefanov, B. B.; Liu, G.; Liashenko, A.; Piskorz, P.; Komaromi, I.; Martin, R. L.; Fox, D. J.; Keith, T.; Alâ€Laham, M. A.; Peng, C. Y.; Nanayakkara, A.; Challacombe, M.; Gill, P. M. W.; Johnson, B.; Chen, W.; Wong, M. W.; Gonzalez, C.; Pople, J. A. et al., Gaussian 09, revision A. 02, Gaussian, Inc., Wallingford CT, 2009.

[7] Becke, A.D. J. Chem. Phys. 1993, 98, 5648.

[8] Hohenberg, P.; Kohn, W. Phys. Rev. B. 1964, 136, 864.

[9] Lee, C.; Yang, W.; Parr, R. G. Phys. Rev. B. 1988, 37, 785.

[10] Frisch, A. et al. Gaussian Inc. GaussView, Version 6;2009.

[11] Jamroz, M. H.; Vibrational Energy Distribution Analysis, VEDA 4 Program, Warsaw, Poland, 2004.

[12] Daina, A.; Michielin, O.; Zoete, V.; SWISSADME online software. 2017.

[13] Bisong, E. (2019). Google Colaboratory. Apress, Berkeley, CA. 59–64, 2019. https://doi.org/10.1007/978-1-4842-4470-8_7.

[14] Pople, J. A.; Schlegel, H. B.; Krishnan, R.; Defrees, D. J.; Binkley, J. S.; Frisch, M. J. et al. Int. J. Quant. Chem. 1981, 20, 269.

[15] Karabacak, M.; Kurt, M.; Cinar, M.; Coruh, A. Mol. Phys. 2009, 107, 253.

[16] Colthup, N. B.; Daly, L. H.; Wiberley, S. E. In Introduction to Infrared and Raman Spectroscopy (New York: Academic Press), 1990.

[17] Chou, K. C. *Biophys. Chem.* 1984, 20, 61.

[18] Frohlich, H. In Biological Coherence and Response to External Stimuli (Berlin: Springer), 1988.

[19] Xu, Y.; Chu, Q.; Chen, D.; Fuentes, A. *Front. Mech. Eng*., 7, 744001,2021.

[20] Fukui, K. *Science* 1982, 218, 747.

[21] Fleming, I. In Frontier Orbitals and Organic Chemical Reactions: John Wiley and Sons, New York, 1976.

[22] Sajan, D.; Joseph, L.; Vijayan, N.; Karabacak, M. *Spectrochim. Acta A, Mol. Biomol. Spectrosc.* 2011, 81, 85.

[23] Thomas, R.; Mary, Y. S.; Resmi, K. S.; Narayana, B.; Sarojini, S. B. K.; Armakovic, S.; Armakovic, S. J.; Vijayakumar, G.; Alsenoy, C. V.; Mohan, B. J. J. Mol. Struct. 2019, 1181, 599.

[24] Chattaraj, P. K.; Sarkar, U.; Roy, D. R. Chem. Rev. 2006, 106, 2065.

[25] Ertl, P.; Rohde, B.; Selzer, P. J. Med. Chem. 2000, 43, 3714.

[26] Murugavel, S.; Ravikumar, C.; Jaabil, G.; Alagusundaram, P. J. Mol. Str. 2019, 1176, 729.

[27] Veber, D. F.; Johnson, S. R.; Cheng, H. Y.; Smith, B. R.; Ward, K. W.; Kopple, K. D. J. Med. Chem. 2002, 45, 2615.

[28] Zhao, Y. H.; Le, J.; Abraham, M. H.; Hersey, A.; Eddershaw, P. J.; Luscombe, C. N.; Boutina, D.; Beck, G.; Sherborne, B.; Cooper I.; Platts, J. A. J. Pharm. Sci. 2001, 90, 749.

[29] Yamashita, S.; Furubayashi, T.; Kataoka, M.; Sakane, T.; Sezaki H.; Tokuda, H. Eur. J. Pharm. Sc. 2000, 10, 195.

[30] Rodić, M. V.; Leovac, V. M.; Jovanović, L. S.; Spasojević, V.; Joksović, M. D.; Stanojković, T.; Matić, I. Z.; Vojinović-Ješić L.S.; Marković, V. Eur. J. Med. Chem. 2016, 115, 75.

[31] Lipinski, C. A.; Lombardo, F.; Dominy, B. W.; Feeney, P. J. Adv. Drug Deliv. Rev. 1997, 23, 3.

[32] Lipinski, C. A. Drug Discov. Today Technol. 2004, 1, 337.

[33] Gadaleta, D.; Vukovic, K.; Toma, C.; Lavado, G. J.; Karmaus, A. L.; Mansouri. K.; Kleinstreuer, N. C.; Benfenati, E.; Roncaglioni, A. J. Cheminf. 2019, 11, 58.

[34] Ajay, Bemis, G. W.; Murcko, M. A.; J. Med. Chem. 1999, 42, 4942.

[35] Kumar, C. P.; Raghu, M. S.; Prathibha, B. S.; Prashanth, M. K.; Kanthimathi, G.; Kumar, K. Y.; Parashuram, L.; Alharthi, F. A. Bioorg. Med. Chem. Letters 2021, 44, 128118.

[36] Spackman, P. R.; Turner, M. J.; McKinnon, J. J.; Wolff, S. K.; Grimwood, D. J.; Jayatilaka, D.; Spackman, M. A. *J. Appl. Crystallography*. 54, 1006, 2021.

[37] Lange O. F., Grubmüller H, *J. Phys. Chem. B*. 110:22842–22852, (2006).

[38] Papaleo E, Mereghetti P, Fantucci P, Grandori R, Gioia LD, *J Mol Graph Model*, 27:889–899, (2009).

[39] Valdés-Tresanco, M. S.; Valdés-Tresanco, M. E.; Valiente, P. A.; Moreno, *E. J. Chem. Theory Comput.* 17, 6281, 2021.